Bearing Fault Numerical Model for the Closed-slot Rotor Submersible Motor*

Zhe Ke[1], *Bokai Guan*[2], *Chong Di*[1], *Jingwen Yan*[1] *and Xiaohua Bao*[1*]

(1. School of Electrical Engineering and Automation, Hefei University of Technology, Hefei 230009, China;
2. School of Electrical and Computer Engineering, The Ohio State University, Columbus OH 43210, USA)

Abstract: A numerical model of the bearing fault of a motor with a closed-slot rotor using the finite element method (FEM) is proposed. The rotor's radial motion can be regarded as static eccentric at the defect time points and healthy at other time points. The frequency of the harmonic component is analyzed corresponding to bearing fault in stator current according to the radial movement of the motor shaft. Moreover, the relative permeability variation region is established to achieve the radial motion of the rotor with bearing fault. Firstly, the relative permeability variation region is established in the health and static eccentric models. Then, the defect time points are estimated and the static eccentricity model by transient field is analyzed. Finally, the relative permeability of the variable region in the static eccentric model is imported into the variable region of the health model at the defect time points. The simulation results show that the air gap flux density of the bearing fault model is different from that of the health model and static eccentric models. In addition, the stator current contains harmonic components of the bearing fault. The analysis results prove the applicability of the proposed model.

Keywords: Bearing fault, finite element method, relative permeability variation region, closed-slot rotor, stator current

1 Introduction

The submersible motor is commonly used in water supply and drainage systems [1-2]. The water-cooled submersible motor with the closed-slot rotor is filled with circulating water inside the motor, enabling the motor to have good heat dissipation performance. Since the motor is filled with water, the water-cooled submersible motor is equipped with guide bearings on both sides of the shaft instead of rolling bearings to bear the radial force of the motor. The supporting force of guide bearings is provided by a rotating water film in the internal clearance, which is different from that of rolling bearings. However, the bearing fault is a critical issue in submersible motors [3-4]. To ensure the safe operation of the motor, it is necessary to study the guide bearing fault mechanism and diagnosis.

Electrical and vibration signal analysis are most commonly used for fault diagnosis [5-7]. Wang et al. [8] constructed the graph mapping spectrum of a vibration signal to diagnose bearing faults. Alabied et al. [9-10] realized the application of empirical mode decomposition (EMD) and ensemble empirical mode decomposition (EEMD) algorithms in fault diagnosis of submersible motors. Xian [11] proposed a motor pump state identification algorithm based on multimodal features and combined it with the XGBoost model to detect the state of a submersible motor under complex operating conditions. But since the submersible motor runs underwater, the vibration signal will be interrupted by the flowing water. Boueri [12] used the vibration analysis method to judge the operation state of the guide bearing, but required additional conditions. The study revealed that the electromagnetic performance of the motor was not affected by the water. It is a feasible bearing fault diagnosis method to analyze the variation of the electromagnetic properties of the motor. Mbo'o et al. [13] developed a fault diagnosis system based on current characteristics generated by frequency selection in the stator current spectrum, which evaluated the fault characteristics by linear discriminant analysis and fault diagnosed by Bayesian classifier. Husna et al. [14] designed a centrifugal pump fault detection system based on

Manuscript received March 30, 2022; revised May 5, 2022; accepted May 20, 2022. Date of publication June 30, 2023; date of current version May 10, 2023.
* Corresponding Author, E-mail: sukz@ustc.edu
* Supported by the National Natural Science Foundation of China (51977055), Major Science and Technology Program of Anhui Province (201903a05020042), and Anhui Province Key Laboratory of Large-scale Submersible Electric Pump and Accoutrements.
Digital Object Identifier: 10.23919/CJEE.2023.000010

motor current characteristic signal.

Nevertheless, bearing fault motor data are required to verify the effectiveness of a method. Damaging the guide bearings of the submersible motor to conduct fault tests is not only expensive but dangerous. There are limited fault models capable of reflecting the electromagnetic response of the motor under the guide bearing fault. Feng et al. [15] proposed a bearing fault model by injecting fault harmonic current into the stator current. However, the radial movement of the rotor was not considered in this model. The rotor of the bearing fault motor will move in the radial direction, resulting in changes in the air gap length [16-17]. Therefore, the bearing fault model can be established by moving the rotor radially. The rotor cannot move radially while rotating axially in the finite element model. The permeability variation regions can be established at the junction of the air gap and rotor, which imitate the radial movement of the rotor in the bearing fault motor. Because the guide bearing fault will lead to the rotor's periodic eccentricity (static eccentricity), the influence of the bearing fault on the motor performance can be considered by periodically changing the relative permeability of these regions.

This study proposes a bearing fault numerical model of the closed-slot rotor submersible motor. In the model, two relative permeability variation regions are created, and the permeability data of bearing fault time points are imported into the regions. The radial air gap flux and stator current of the bearing fault model reveal unique characteristics compared with the health and static eccentric models. Furthermore, the variable regions and fault time points can be defined according to the characteristics of simulated bearing faults.

2 Characteristic analysis of motor eccentricity and guide bearing fault

The guide bearings, which are mounted on the upper and lower ends of the shaft, bear the radial force of the motor in the wet submersible motor. The mechanical structure of the guide bearing is shown in Fig. 1. The guide bearing structure includes a bearing shell, bush, and flow hole; moreover, there is a gap between the bearing shell and bush. As the shaft rotates, a rotating water film provides radial support between the bearing shell and bush. The radial force is borne by the guide bearings in the submersible motor, hence bearing fault will seriously affect safe operation of the motor.

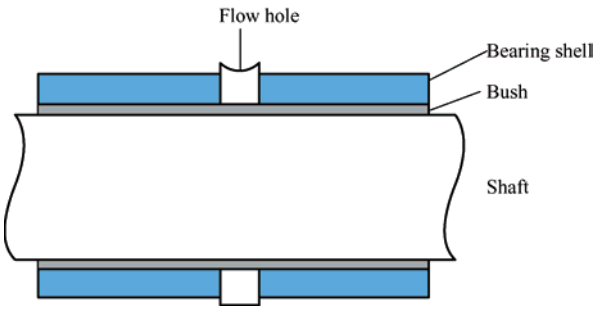

Fig. 1 Structure of guide bearing

However, temperature changes caused by motor operation and shutdown lead to larger sealing clearance. When the working environment of the submersible motor contains impurities, such as dirt and sand, the impurities easily find their way into the motor through the gap. In addition, the rotating operation of the motor may also form a small number of particle impurities. Sand and other impurities will enter the water film of the guide bearing with the circulating water. As a result, the balance of the water film is destroyed, and the impurities collide with the guide bearing shell and bush, which finally leads to the failure crack and defect points in the guide bearing. Fig. 2 shows the guide bearing of the submersible motor with a cracked inner wall. Cracks are marked by the dash line and friction marks can be seen in the black circle.

Fig. 2 Schematic diagram of the guide bearing mechanical structure

The thickness of the water film change when defects exist in the inner and outer walls of the bearing and bush. Therefore, the radial support force provided by the water film will also change. The circumstances will lead to static eccentricity of the motor rotor. The analysis of a static eccentric motor is a prerequisite for the fault analysis of motor guide bearing.

2.1 Length of air gap in the static eccentric motor

Motor eccentricity occurs when the motor rotor, stator, and rotary centers do not coincide. Types of motor eccentricities include static, dynamic, and mixed [18]. The two most basic are static and dynamic eccentricity [19]. Fig. 3 shows the radial section of static and dynamic eccentric motors; the dot represents the center of rotation of the rotor. For the static eccentric motor, the geometric centers of the rotor and stator do not coincide, and the geometric center and rotation centers of the rotor are consistent. Simultaneously, the air gap length of the motor is non-uniform, but will not change. For the dynamic eccentric motor, the geometric center of rotor and stator coincide, but the rotor rotation center is offset, and the air gap length varies regularly with time. Mixed eccentricity occurs when the motor's static and dynamic eccentricity coexist. The geometric centers of the rotor and stator of the mixed eccentric motor do not coincide, and the rotation center does not coincide with the two geometric centers. The following section will discuss the motor's air gap flux density for a static eccentric induction motor.

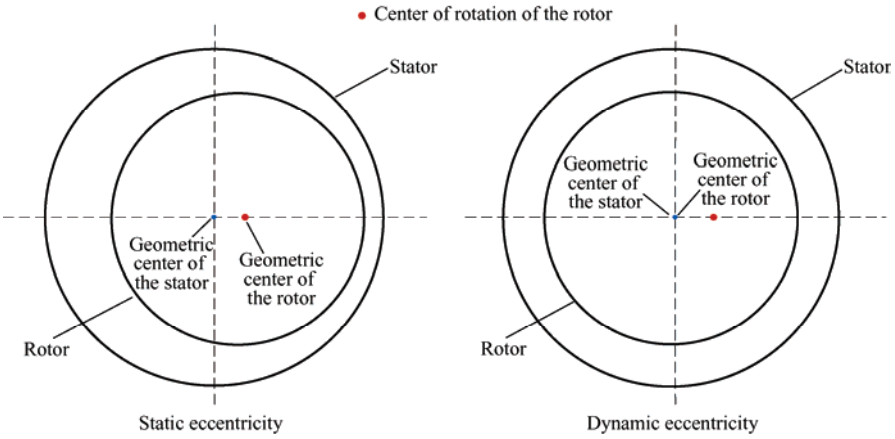

Fig. 3 Static and dynamic eccentric radial section diagram of the motor

The motor's static eccentricity fault is attributable to the rotor geometric center point being different from that of the stator, and the rotary center of the rotor rotary center coinciding with the geometric center [20]. A coordinate system was established with the stator geometric center as the origin, as shown in Fig. 4. O_S and O_R are the geometric centers of the stator and rotor; O_R is also the rotation center. θ is the angle between the selected position and the coordinate axis and χ is the rotor offset distance caused by static eccentricity. The inner and outer diameter of the motor stator are denoted R_s and R_r. Essentially, $O_SB=R_s$ and $O_RA=R_r$. According to the law of cosines

$$\begin{cases} {O_R}^2 = {O_S O_R}^2 + {O_S A}^2 - 2O_S O_R \cdot O_S A \cdot \cos\theta \\ {R_r}^2 = \chi^2 + {O_S A}^2 - 2\chi \cdot O_S A \cdot \cos\theta \end{cases} \quad (1)$$

The length of O_SA can be estimated by solving the above equation

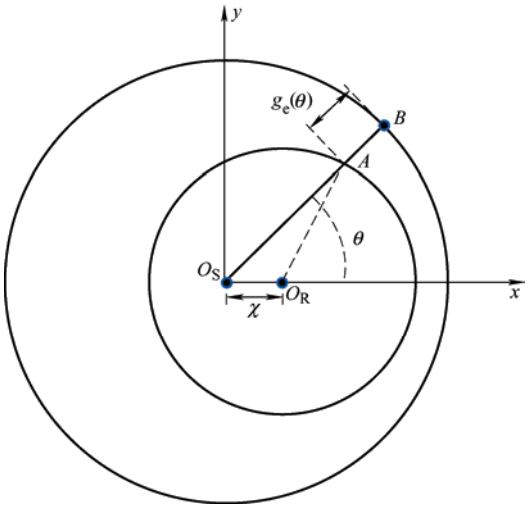

Fig. 4 Air gap length of the static eccentric motor

$$O_S A = \chi \cdot \cos\theta + \sqrt{{R_r}^2 + \chi^2 \cdot \cos^2\theta - \chi^2} \quad (2)$$

The outer diameter of the rotor is much larger than the offset distance caused by the eccentricity, and Eq.

(2) can be simplified as

$$O_S A \approx \chi \cdot \cos\theta + R_r \tag{3}$$

The motor air gap length $g_e(\theta)$ is

$$g_e(\theta) = O_S B - O_S A = R_s - (\chi \cdot \cos\theta + R_r) = g_0 - \chi\cos\theta \tag{4}$$

where g_0 is the air gap length in a healthy motor.

2.2 Length of air gap in the guide bearing fault motor

The primary fault type of the guide bearing of the submersible motor is cracks or defects in the inner wall of the bearing bush, which causes imbalance of the water film. The water film imbalance will cause the rotor to wobble, as shown in Fig. 5. When the motor shaft rotates at the defect point, the rotor is in a static eccentric state. After leaving the defect point, the rotor returns to its original position. Fig. 6 shows the submersible motor's rotor position change with the guide bearing fault.

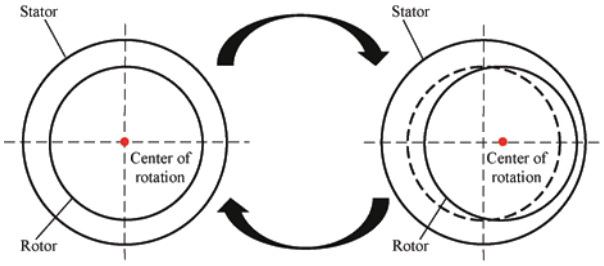

Fig. 5 Change of the submersible motor's rotor position with the guide bearing fault

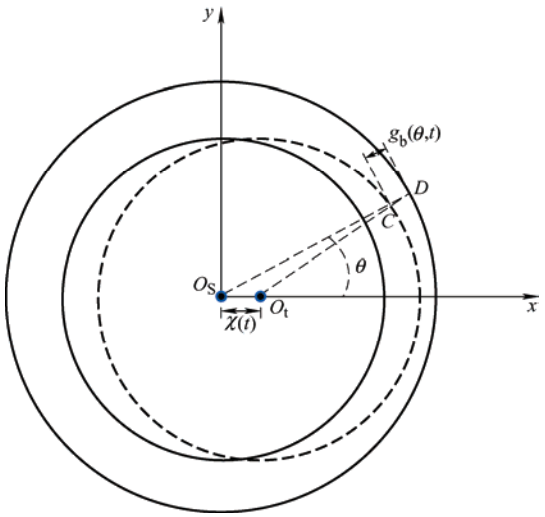

Fig. 6 Air gap length diagram of the static eccentric motor

The radial displacement change is approximated as a pulse change, and the deviation distance of the rotation center $\chi(t)$ is

$$\chi(t) = \chi_b \delta\left(t - \frac{k}{f_b}\right) \quad k = 0,1,2,\cdots,n \tag{5}$$

where χ_b is the maximum eccentric distance caused by bearing fault and f_b is the characteristic frequency of the guide bearing fault. The air gap length of the motor with guide bearing fault is determined as

$$g_b(\theta,t) = g_0 - \chi_b \delta\left(t - \frac{k}{f_b}\right)\cos\theta \tag{6}$$

In this case, the air gap permeance is [21]

$$\lambda_b(\theta,t) = \frac{\lambda(\theta,t)}{1 - \varepsilon_b \delta\left(t - \frac{k}{f_b}\right)\cos\theta} \tag{7}$$

$$\varepsilon_b = \frac{\chi_b}{g_0} \tag{8}$$

where $\lambda(\theta,t)$ is the air gap permeance in the healthy motor and ε_b is the eccentricity ratio. Eq. (7) can be simplified to

$$\lambda_b(\theta,t) = \lambda(\theta,t)\left[1 + \varepsilon_b \delta\left(t - \frac{k}{f_b}\right)\cos\theta\right] \tag{9}$$

The impulse function in the above equation can be transformed into the Fourier series form as

$$\delta\left(t - \frac{k}{f_b}\right) = c_0 + 2\sum_{n=1}^{+\infty} f_b \cos(n\omega_b t) \tag{10}$$

where c_0 is a constant and $\omega_b = 2\pi f_b$. The air gap permeance in the motor with a guide bearing fault can be expressed by

$$\begin{aligned}\lambda_b(\theta,t) &= \lambda(\theta,t)\{1 + \varepsilon_b[c_0 + 2\sum_{n=1}^{+\infty} f_b \cos(n\omega_b t)]\cos\theta\} = \\ &\lambda(\theta,t)[1 + \varepsilon_b \cdot c_0 \cos\theta + \varepsilon_b \sum_{n=1}^{+\infty} f_b \cos(n\omega_b t + \theta) + \\ &\varepsilon_b \sum_{n=1}^{+\infty} f_b \cos(n\omega_b t - \theta)]\end{aligned} \tag{11}$$

2.3 Air gap flux density and stator current of the motor with guide bearing fault

Next, the air gap flux density of the motor with a guide bearing fault is analyzed. The magnetomotive force (MMF) of the healthy motor is determined as [22]

$$f(\theta,t) = f_p(\theta,t) + \sum_{\nu} f_\nu(\theta,t) + \sum_{\mu} f_\mu(\theta,t) \tag{12}$$

where $f_p(\theta,t)$ is the synthetic fundamental MMF; $f_\nu(\theta,t)$ and $f_\mu(\theta,t)$ are the ν-order stator and μ-order rotor harmonic MMFs. In the induction machine, the MMF of each item in Eq. (12) can be expressed as

$$\begin{cases} f_p(\theta,t)=F_p\cos(p\theta-\omega_1 t-\varphi_0) \\ f_\nu(\theta,t)=F_\nu\cos(\nu\theta-\omega_1 t-\varphi_\nu) \\ f_\mu(\theta,t)=F_\mu\cos(\mu\theta-\omega_\mu t-\varphi_\mu) \end{cases} \tag{13}$$

where F_p, F_ν, and F_μ are the magnitudes of the corresponding order of the fundamental, stator, and rotor harmonic MMFs. p is the polar logarithm of the motor, $\omega_1=2\pi f$ is the rotational angular velocity of the power supply, and f is the frequency of the power supply. φ_0, φ_ν and φ_μ are the corresponding phase angles. ω_μ is

$$\omega_\mu=\omega_1\left[1+k_\mu\frac{Z_2}{p}(1-s)\right] \quad k_\mu=\pm1,\pm2,\cdots,\pm n \tag{14}$$

where s is the slip of the motor.

The air gap flux density of the motor with guide bearing failure is

$$\begin{aligned} B(\theta,t)=f(\theta,t)\lambda_{\mathrm{b}}(\theta,t)=&F_p\lambda(\theta,t)\cos(p\theta-\omega_1 t-\varphi_0)+\\ &\sum_\nu F_\nu\lambda(\theta,t)\cos(\nu\theta-\omega_1 t-\varphi_\nu)+\\ &\sum_\mu F_\mu\lambda(\theta,t)\cos(\mu\theta-\omega_\mu t-\varphi_\mu)+\\ &\frac{\varepsilon_{\mathrm{b}}c_0}{2}F_p\lambda(\theta,t)\cos[(p\pm1)\theta-\omega_1 t-\varphi_0]+\\ &\frac{\varepsilon_{\mathrm{b}}c_0}{2}\sum_\nu F_\nu\lambda(\theta,t)\cos[(\nu\pm1)\theta-\omega_1 t-\varphi_\nu]+\\ &\frac{\varepsilon_{\mathrm{b}}c_0}{2}\sum_\mu F_\mu\lambda(\theta,t)\cos[(\mu\pm1)\theta-\omega_1 t-\varphi_\mu]+\\ &\varepsilon_{\mathrm{b}}f_{\mathrm{b}}\sum_{n=1}^{+\infty}F_p\lambda(\theta,t)\cos[(p\pm1)\theta-\omega_1 t\pm n\omega_{\mathrm{b}}t-\varphi_0]+\\ &\varepsilon_{\mathrm{b}}f_{\mathrm{b}}\sum_\nu\sum_{n=1}^{+\infty}F_\nu\lambda(\theta,t)\cos[(\nu\pm1)\theta-\omega_1 t\pm n\omega_{\mathrm{b}}t-\varphi_\nu]+\\ &\varepsilon_{\mathrm{b}}f_{\mathrm{b}}\sum_\mu\sum_{n=1}^{+\infty}F_\mu\lambda(\theta,t)\cos[(\mu\pm1)\theta-\omega_1 t\pm n\omega_{\mathrm{b}}t-\varphi_\mu]+\\ &\varepsilon_{\mathrm{b}}f_{\mathrm{b}}\sum_{n=1}^{+\infty}F_p\lambda(\theta,t)\cos[(p\mp1)\theta-\omega_1 t\pm n\omega_{\mathrm{b}}t-\varphi_0]+\\ &\varepsilon_{\mathrm{b}}f_{\mathrm{b}}\sum_\nu\sum_{n=1}^{+\infty}F_\nu\lambda(\theta,t)\cos[(\nu\mp1)\theta-\omega_1 t\pm n\omega_{\mathrm{b}}t-\varphi_\nu]+\\ &\varepsilon_{\mathrm{b}}f_{\mathrm{b}}\sum_\mu\sum_{n=1}^{+\infty}F_\mu\lambda(\theta,t)\cos[(\mu\mp1)\theta-\omega_1 t\pm n\omega_{\mathrm{b}}t-\varphi_\mu] \end{aligned} \tag{15}$$

where s is the slip of the motor.

According to Eq. (15), the harmonic component caused by the guide bearing fault will appear in its air gap flux density. The order and frequency of the harmonic component will change, and the frequency change is related to the frequency of the power supply and bearing fault. The change of air gap magnetic field will distort the stator current, and the harmonic component of the air gap magnetic density caused by bearing fault will induce a corresponding harmonic component in the stator current [23], whose frequency is

$$F_{\mathrm{b}}=\left\|f\pm kf_{\mathrm{b}}\right\| \qquad k=1,2,\cdots,n \tag{16}$$

3 Bearing fault numerical model

The bearing fault will cause complex periodic static eccentricity of the motor rotor. In the induction motor, the magnetic field energy is mainly concentrated in the air gap, and the change of the air gap magnetic field greatly influences the motor's electromagnetic performance. This study presents a simplified bearing fault numerical model for the closed-slot rotor. The model simulates bearing fault by periodically changing the rotor into static eccentricity with the finite element method (FEM).

The length of the air gap changes because of the rotor's static eccentricity. Similarly, the air gap length changes periodically because of the bearing fault. The electromagnetic performance of the motor will change, corresponding to the change of the air gap length. In the finite element numerical model of the motor, the radial position of the rotor is changed by creating the permeability variation regions.

The model creates two relative permeability variation regions in the rotor edge and air gap. Fig. 7 shows the relative permeability variation regions. Circle 1, 2, and 3 represent the inner diameter of the stator, outer diameter of the healthy rotor, and outer diameter of the static eccentric rotor; O_{S} is the center of circles 1 and 2 and O_{E} is the center of circle 3. The non-coincidence parts of circles 1 and 2 are the relative permeability variation regions, which are marked region 1 and 2 as shown. When the rotor is turned to the defect point, the position of the rotor will change from circle 1 to 2, and the rotor will turn back after passing this point. In the model of the healthy motor, the material of region 1 is silicon steel, and region 2 is air. In contrast, region 1 is air, and region 2

is silicon steel in the model of the static eccentric motor. The health and static eccentric motor models need to be established in advance to obtain the permeability value of the relative permeability variation regions in the two cases. The regions should be set in the same position. The relative permeability of the magnetic conductivity change region at each time point can be obtained by analyzing the two models. The following steps establish the bearing fault numerical model, as shown in Fig. 8.

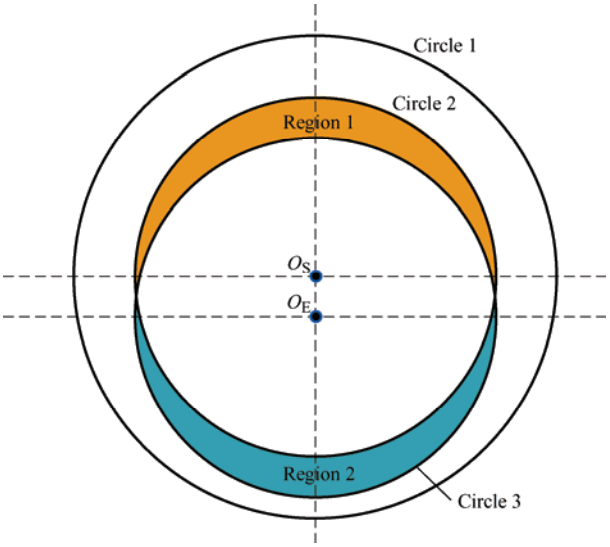

Fig. 7 Location diagram of relative permeability variation regions

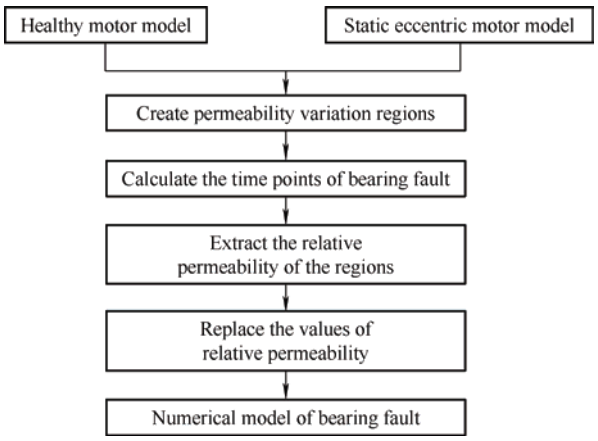

Fig. 8 Establishment of bearing fault model

(1) Employ FEM to establish two 2-D models of healthy and static eccentric motors that contain relative permeability variation regions.

(2) Calculate time points of bearing fault.

(3) Conducts finite element analysis of the static eccentric model using the transient field. Then extract the relative permeability of the regions at the defect time points.

(4) Replace the relative permeability values in the health model with the values obtained in Step (3), which are at the exact location and time points.

By following the above steps, a numerical model of the bearing fault is established. The stator current of the bearing fault can be qualitatively analyzed with this model.

4 Simulation and analysis

4.1 Motor parameters and numerical model

This study uses a 55 kW closed-slot rotor submersible motor as an example. The motor parameters are shown in Tab. 1. It is assumed that the motor guide bearing inner wall has one defect point which establishes the fault's numerical model.

Tab. 1 Parameter of closed-slot rotor submersible motor

Parameter	Value
Rated power/kW	55
Number of pole-pairs	2
Rated voltage/V	380
Rated frequency/Hz	50
Outer diameter of stator/mm	400
Inner diameter of stator/mm	225
Inner diameter of rotor/mm	85
Length of iron core/mm	180
Length of air gap/mm	1.2
Number of stator slots	36
Number of rotor slots	42

Firstly, two 2-D models of the submersible motor are established, corresponding to the health and static eccentric states. To simplify the analysis, the rotor eccentricity caused by the bearing fault is set as 0.5 mm. Therefore, the static eccentric model's offset value is also 0.5 mm. Secondly, the time points of bearing fault are estimated. The speed of the motor is 1 440 rad/min, and there is only one defect point on the inner wall of the bearing shell. Then the rotation frequency of the shaft is 24 Hz. The motor rotor repeats the process from healthy to eccentric to healthy every 1/24 s. The fault duration is 0.000 2 s, and the bearing fault characteristic frequency is 24 Hz. Thirdly, the relative permeability of regions 1 and 2 at the bearing fault time point are extracted. To simplify the model, this experiment extracts the relative permeability of the broadest part of the regions which is 320. Finally, the relative permeability data of the two regions in the healthy motor are replaced with extracted data every 1/24 s starting at 0.25 s.

The experiment established three models: bearing fault, health, and static eccentric. Fig. 9 shows the bearing fault numerical model of the single point defect. The left half of the model in Fig. 9a displays the meshing of the motor model. Figs. 9b and 9c show regions 1 and 2 marked. Meanwhile, the healthy and static eccentric motor models were established to compare the changes in electromagnetic performance with the bearing fault model.

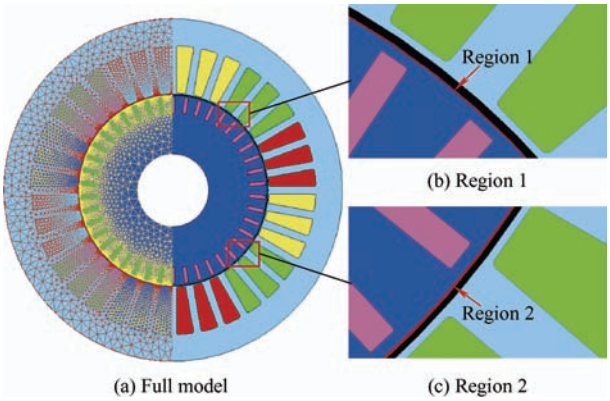

Fig. 9 FEM numerical model of single point bearing fault

4.2 Analysis

Finite element analysis of the three models is conducted by transient field. Because the bearing fault model periodically changes the air gap length, its radial air gap flux density is bound to change [24]. Fig. 10 shows the 3-D waveform of the radial air gap flux density in the guide bearing fault model, with the acquisition time ranging from 0.5 s to 0.52 s.

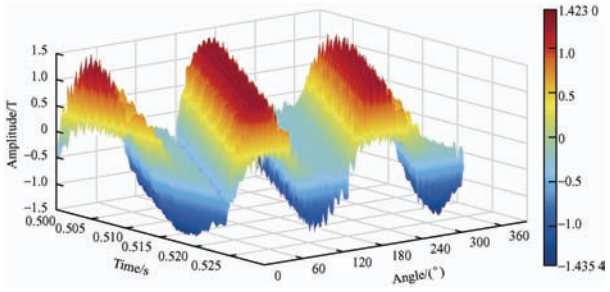

Fig. 10 Air gap flux density waveform of the motor model with guide bearing fault

Fig. 11 shows the 2-D spectrum diagram of air gap flux density of the bearing fault. The harmonic component is invisible for better spectrum analysis, with an amplitude of less than 0.02 in the figure. The amplitude of the fundamental wave of the air gap flux density is 0.629 5, and the −34th and 38th harmonics are the first-order stator tooth harmonics with amplitudes of 0.286 9 and 0.142 7. The 40th and 44th harmonics are the first-order rotor tooth harmonics with amplitudes of 0.070 7 and 0.065 2. –10th, –22nd, 14th, and 26th harmonics are phase band harmonics. Then, the air gap flux density of the guide bearing fault model is compared with that of the healthy and static eccentric motor models, and the differences between the models are analyzed.

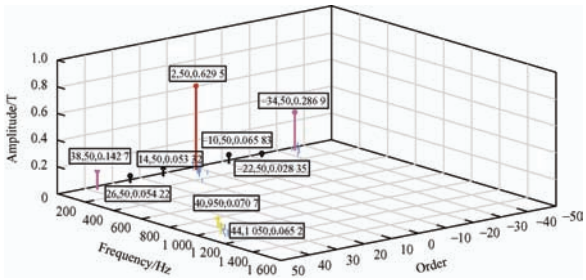

Fig. 11 Spectrum diagram of the radial air gap flux density in the bearing fault model

The 2-D FFT is performed for the air gap flux density of the healthy and static eccentric motor models, and the spectral results are compared with the bearing fault results. The comparison of the air gap flux density harmonic amplitudes of the three models is shown in Fig. 12. In order of priority, the data on the left is the order and amplitude of the air gap flux density harmonics of the bearing fault model. The middle is the healthy model, and the right is the static eccentric model. Clearly, the static eccentric model's the amplitude of the air gap magnetic density fundamental wave is smaller than that of the health model but larger than that of the bearing fault model. The amplitudes of most harmonic components are larger than that of the two models. Rotor static eccentricity will change the harmonic order of the air gap magnetic density, increase the amplitude of the harmonic component and decrease the amplitude of the fundamental wave [25]. The air gap magnetic density fundamental wave amplitude in the bearing fault motor model is slightly smaller than that in the static eccentric model. Similar to the static eccentric model, the amplitudes of the –34th and 38th (stator first tooth harmonics) order harmonics of the air gap flux density increase in the bearing fault model. However, the 40th and 44th order harmonics (rotor first tooth harmonics) amplitudes decrease, distinguishing

static eccentric fault from the bearing fault.

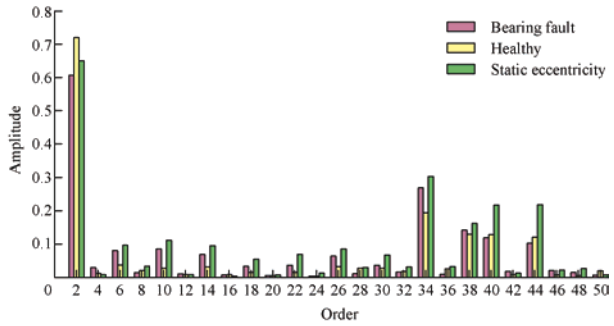

Fig. 12 Specific order component of the air gap magnetic density of the three models

According to the theoretical analysis of the second part, the stator current will have the corresponding harmonic component when the bearing fault exists in the motor. The stator current waves of the three models are shown in Fig. 13. To facilitate observation of the difference, the three current waveforms are staggered. The *x*-axis in the figure is not the real-time axis. The stator current of the bearing fault model appears slightly distorted, which is marked in circle.

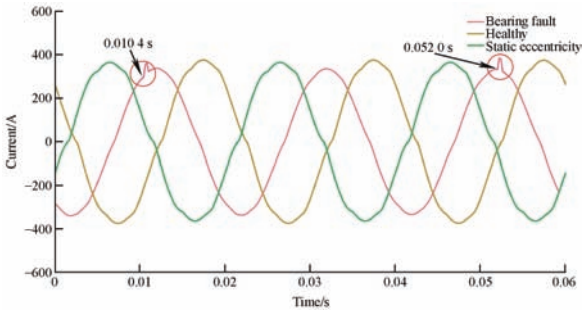

Fig. 13 Stator current waves of the three models

Furthermore, the two distortions in stator current occur at 0.010 4 s and 0.052 0 s. The time between the two current distortions is approximately 1/24 s, which is identical to the bearing fault period time. In addition, the stator current peak value of the bearing fault model is smaller than that of the other two models. Then, the FFT analyzes the stator current of the bearing fault model. Fig. 14 demonstrates the spectrum diagram of the stator current. In the figure, we hide the components with amplitudes less than 0.5 for observation and analysis. Fig. 14b is the local enlarged drawing of Fig. 14a, marked by the rectangle with a dotted line. In Fig. 14a, the fundamental, third harmonic, and fifth harmonic components of the stator current are 337, 4.975, and 3.823. There are two harmonic components with amplitudes larger than 0.5 around the fundamental wave. The stator current contains 46 Hz and 48 Hz components, which are the $||f - 3f_b||$ and double frequency components of bearing fault frequency. Compared with the fundamental wave amplitude of the stator current, the current distortion caused by the bearing fault is slight, and the amplitude of the component corresponding to the fault characteristic frequency is also small in the spectrum diagram. However, all of them can be displayed in the spectrum diagram. Therefore, the fault of the motor guide bearing can be diagnosed by detecting the distortion in the stator current and its corresponding frequency.

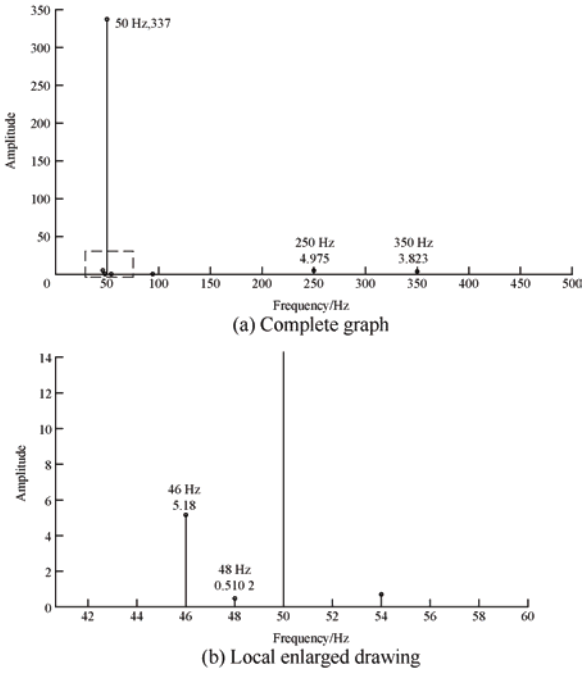

Fig. 14 Stator current spectrum diagram of bearing fault model

The above results prove that the bearing fault motor model is different from the healthy motor and static eccentric motor models in air gap flux density and stator current. In addition, it verifies the validity of the model and the fault characteristic frequency component in the stator current. Finally, provides a new theoretical basis for distinguishing motor guide bearing fault from static eccentric fault.

5 Conclusions

(1) This study presents a novel numerical model of a submersible motor with guide bearing fault. In the model, the radial mechanical movement of the rotor with bearing fault is realized by creating a relative permeability variation region. This model can be used

to analyze the electromagnetic characteristics of the motor with guide bearing faults.

(2) The variation characteristics of air gap flux density and stator current under guide bearing fault are deduced theoretically. The results show that the order and frequency of air gap flux density will change due to the guide bearing fault, and the characteristic component of the bearing fault will be induced in the stator current. The analysis of simulation results verifies the effectiveness of the proposed model.

(3) This method can be used to establish the fault model of rolling bearings. Meanwhile, the results reflect the different effects of the bearing and static eccentric fault on the electromagnetic performance of the motor, which can be used as the basis to distinguish two kinds of faults in fault diagnosis.

(4) The numerical model can be applied to the field of bearing fault diagnosis to prove the effectiveness of diagnosis technology and avoid the repetition of actual experiments. However, the numerical model of the bearing fault constructed in this study applies to the motor with the closed-slot rotor. Subsequent research should aim at the establishment of the bearing fault motor model with an open-slot rotor.

References

[1] H Deng, B Xue, D Xu, et al. Speed estimation for submersible motor based on Elman neural network. *Proceedings of the CSEE*, 2007, 27(24): 102-106.

[2] Y Fang, X Bao, Q Lv, et al. Analysis of electromagnetic force distribution on end winding of electrical submersible motor during starting transient operation. *IEEE Transactions on Magnetics*, 2013, 49(10): 5341-5345.

[3] Z Yuan, F Song, R Dou. Research on bearing fault diagnosis of submersible pump motor based on LMD and SVDD. *IOP Conference Series: Materials Science and Engineering*, 2020, 711(1): 012041.

[4] Y Yang. A high-dimensional and small-sample submersible fault detection method based on feature selection and data augmentation. *Sensors*, 2022, 22(1): 204.

[5] S E Khil, I Jlassi, A M Cardoso, et al. Diagnosis of open-switch and current sensor faults in PMSM drives through stator current analysis. *IEEE Transactions on Industry Applications*, 2019, 55(6): 5925-5937.

[6] X Liang. Temperature estimation and vibration monitoring for induction motors and the potential application in electrical submersible motors. *Canadian Journal of Electrical and Computer Engineering*, 2019, 42(3): 148-162.

[7] S Zhang, F Ye, B Wang, et al. Few-shot bearing fault diagnosis based on model-agnostic meta-learning. *IEEE Transactions on Industry Applications*, 2021, 57(5): 4754-4764.

[8] T Wang, Z Liu, G Lu, et al. Temporal-spatio graph based spectrum analysis for bearing fault detection and diagnosis. *IEEE Transactions on Industrial Electronics*, 2021, 68(3): 2598-2607.

[9] S Alabied, U Haba, A Daraz, et al. Empirical mode decomposition of motor current signatures for centrifugal pump diagnostics. *2018 24th International Conference on Automation and Computing* (*ICAC*), September 06-07, 2018, Newcastle Upon Tyne, UK. IEEE, 2018: 1-6.

[10] W Dong, Y Cai, K L Tsui. Making EEMD more effective in extracting bearing fault features for intelligent bearing fault diagnosis by using blind fault component separation. *Journal of Intelligent & Fuzzy Systems Applications in Engineering & Technology*, 2018, 34(6): 3429-3441.

[11] D Xian. State recognition of motor pump based on multimodal homologous features and XGBoost. *2021 IEEE International Conference on Manipulation, Manufacturing and Measurement on the Nanoscale* (*3M-NANO*), 2021: 231-236.

[12] B F Boueri. Identifying a guide bearing rub using vibration analysis. *Hydro Review*, 2014, 33(4): 10-12, 14, 16.

[13] C P Mbo'o, K Hameyer. Fault diagnosis of bearing damage by means of the linear discriminant analysis of stator current features from the frequency selection. *IEEE Transactions on Industry Applications*, 2016, 52(5): 3861-3868.

[14] A Husna, K Indriawati, B L Widjiantoro. Discriminant feature extraction of motor current signal analysis and vibration for centrifugal pump fault detection. *2021 International Conference on Instrumentation*, *Control*, *and Automation* (*ICA*), 2021: 207-212.

[15] B Feng, C Qiu, C Xu. A diagnosis method for motor bearing fault based on harmonic injection. *The 6th International Conference on Machinery*, *Materials Science and Engineering Applications*, 2016.

[16] R R Schoen, T G Habetler, F Kamran, et al. Motor bearing damage detection using stator current monitoring. *IEEE Transactions on Industry Applications*, 1995, 31(6): 1274-1279.

[17] M Blodt, P Granjon, B Raison, et al. Models for bearing damage detection in induction motors using stator current monitoring. *IEEE Transactions on Industrial Electronics*, 2008, 55(4): 1813-1822.

[18] Y Wang, K Liu, W Hua, et al. Analysis and detection of rotor eccentricity in permanent magnet synchronous machines based on linear hall sensors. *IEEE Transactions*

on Power Electronics, 2022, 37(4): 4719-4729.

[19] J Shin, Y Park, B L Sang. Flux-based detection and classification of induction motor eccentricity, rotor cage, and load defects. *IEEE Transactions on Industry Applications,* 2021, 57(3): 2471-2480.

[20] S Zuo, Z Liu, S Hu. Vibration reduction of switched reluctance motor under static eccentricity with optimized current harmonic. *IET Electric Power Applications*, 2020, 14(8): 1480-1487.

[21] P Frauman, A Burakov, A Arkkio. Effects of the slot harmonics on the unbalanced magnetic pull in an induction motor with an eccentric rotor. *IEEE Transactions on Magnetics*, 2007, 43(8): 3441-3444.

[22] H Asgharpour-Alamdari, Y Alinejad-Beromi, H Yaghobi. Improvement of induction motor operation using a new winding scheme for reduction of the magnetomotive force distortion. *IET Electric Power Applications*, 2017, 12(3): 323-331.

[23] B M Ebrahimi, M Javan Roshtkhari, J Faiz, et al. Advanced eccentricity fault recognition in permanent magnet synchronous motors using stator current signature analysis. *IEEE Transactions on Industrial Electronics*, 2014, 61(4): 2041-2052.

[24] L Frosini, C Harlisca, L Szabo. Induction machine bearing fault detection by means of statistical processing of the stray flux measurement. *IEEE Transactions on Industrial Electronics*, 2015, 62(3): 1846-1854.

[25] D Kim, H Kim, J Hong, et al. Estimation of acoustic noise and vibration in an induction machine considering rotor eccentricity. *IEEE Transactions on Magnetics*, 2014, 50(2): 857-860.

Zhe Ke was born in Wuhu, China, in 1996. He received the B.Eng. degree in Electrical Engineering from Nantong University, Nantong, in 2018. He is currently pursuing the master's degree in Electrical Engineering with the School of Electrical Engineering and Automation, Hefei University of Technology, Hefei, China.

His current research interests mainly include motor bearing fault diagnosis and and cause analysis.

Bokai Guan was born in Hubei, China, in 1998. He received the B. Eng. degree from Hefei University of Technology, Hefei, China, in 2020. He joined the Department of Electrical and Computer Engineering, The Ohio State University, Columbus, OH, USA, as a postgraduate. His current research interests include bearing fault diagnosis and machine learning.

Chong Di was born in China. He received the B.Eng. and M.Eng. degrees from Hefei University of Technology, Hefei, China, in 2014 and 2017, respectively, and the Doctor of Science (D.Sc.) degree from Lappeenranta-Lahti University of Technology (LUT), Finland, in 2020, all in Electrical Engineering.

He is currently a Researcher in the Department of Electrical Engineering, Hefei University of Technology, Hefei, China. His research mainly concerns high-speed electrical machines and modelling of electrical machines on the open-source platform.

Jingwen Yan gotten the B.Eng. degree in Material Science from Soochow College, Suzhou, China, in 2018. She is right now seeking after the Ph.D. degree with the School of Electrical Designing and Computerization, Hefei College of Innovation, Hefei, China.

Her current research interests include motor electromagnetic design, iron loss calculation and analysis, motor harmonic analysis.

Xiaohua Bao was born in China. He received his B.Eng., M.Eng., and Ph.D. degrees in Electrical Engineering from the Hefei University of Technology, Hefei, China, in 1996, 2002, and 2008, respectively. He joined the School of Electrical Engineering and Automation, Hefei University of Technology, where he became a Professor in 2012. He was a Visiting Scholar with the Virginia Polytechnic Institute and State University, Blacksburg, VA, USA.

His current research interests include motor design, magnetic field analysis, and finite-element analysis.